Continuous wave-Nd: yttrium–aluminum–garnet laser welding of AM60B magnesium alloy

M. Pastor, H. Zhao, and T. DebRoy
Department of Materials Science and Engineering, The Pennsylvania State University, University Park, Pennsylvania

(Received 29 October 1999; accepted for publication 8 March 2000)

This study shows that the formation of macroporosity and overfill in the weld pool were the most pronounced problems during continuous wave Nd:yttrium–aluminum–garnet laser welding of AM60B die cast magnesium alloy. The influences of various welding parameters on the formation of porosity and overfill were investigated with particular emphasis on the mechanism and prevention of porosity formation. It was found that the macro pores in the weld pool were mainly formed by the expansion and coalescence of the preexisting pores in the base metal. The amount of macroporosity in the weld pool could be reduced to approximately that in the base metal by reducing heat input, i.e., by increasing welding speed and decreasing laser power. Increasing the beam defocusing did not reduce porosity in the weld metal until the beam was highly defocused and a shallow weld pool, characteristic of conduction mode welding was obtained. Overfill was observed for deep penetration autogenous welds and its formation could be attributed to porosity formation and the resulting displacement of the liquid metal over the top surface of the workpiece. [S1042-346X(00)00103-0]

Key words: porosity, magnesium alloy, laser welding, overfill, weld defects, grain size, microhardness

I. INTRODUCTION

Because of their low weight and high specific strength (tensile strength divided by specific gravity), magnesium alloys show particular promise for the construction of lightweight structures. Most magnesium alloys are used for parts that operate at high rotational speeds in order to minimize inertial forces. Current structural applications of magnesium alloys include industrial machinery, automotive components, and aerospace equipment. Although joining of these alloys are important for their use, very little work has been reported on the laser welding of these alloys.[1–4] It is known that magnesium alloys are difficult to weld due to pore formation[1–3] and liquation cracking.[4]

Liquid magnesium has a much larger solubility of hydrogen than solid magnesium.[5] Therefore, similar to aluminum alloys, hydrogen porosity is an important concern for the welding of magnesium alloys.[6–10] In addition, the imperfect collapse of the keyhole[11–16] and turbulent flow in the weld pool[17] are possible causes of macroporosity formation in the weld metal during laser welding. Weisheit *et al.*[2] reported that die cast magnesium alloys were more prone to porosity formation than cast or wrought magnesium alloys. However, the mechanism of pore formation in die cast magnesium alloys is not well understood.

Previous work[15] on the laser welding of automotive aluminum alloys has shown that macroporosity in the welded joints could be controlled by appropriate selection of welding variables. Furthermore, a large window of operating parameters existed to achieve defect free, structurally sound, and reliable welds. Such information for laser welding of magnesium alloys is not generally available.

The goal of this research is to examine the influences of welding speed, laser power, and beam defocusing on the laser welding of AM60B die cast magnesium alloy. Its specific strength of about 122 MPa compares favorably with 103 MPa for aluminum alloy 5083 and about 45 MPa for low carbon steel. Excellent specific strength, good elongation, toughness and yield strength make this alloy an attractive candidate for numerous potential applications if the alloy can be welded satisfactorily. The results reported here focus on the porosity formation during laser welding with emphasis on understanding the mechanisms of pore formation. It is hoped that the results can serve as a basis for the reduction of porosity in the weld metal.

II. EXPERIMENT

Bead-on-plate autogenous welds were produced on 2- and 6-mm-thick plates of AM60B magnesium die cast alloy.

TABLE I. Chemical composition of alloy AM60B.

Al (wt %)	Cu (wt %)	Fe (wt %)	Mn (wt %)	Ni (wt %)	Si (wt %)	Zn (wt %)	Mg (wt %)
5.22	<0.01	<0.01	0.26	<0.01	0.04	0.05	Balance

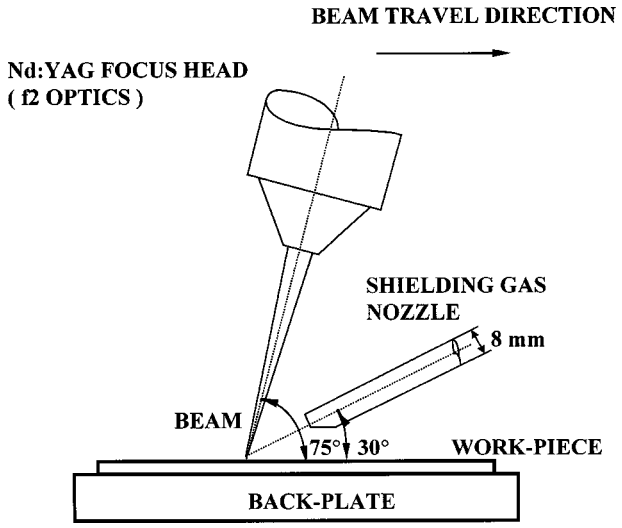

FIG. 1. Nd:YAG laser welding arrangement.

The composition of an AM60B sample was determined by spectrochemical characterization and the results are presented in Table I. The sample dimensions were 28 mm wide, 150 mm long, and either 2.0 or 6.0 mm thick. Prior to welding, the samples were ground with 400 grit SiC paper and cleaned with acetone. Figure 1 schematically shows the experimental arrangement. The laser beam was delivered using a 600 μm diameter fiber of fused silica to a f2 focus optics manipulated through a micropositioning stage mounted on a linear translation device. The focal length of the f2 optics for Nd:yttrium–aluminum–garnet (YAG) laser is 77.7 mm and the beam radius at the focal point is 300 μm. The beam was provided at a 75° forward angle relative to the work-piece to prevent damage to the optics due to backreflection. An ancillary copper nozzle having a 8.0 mm inside diameter was utilized to provide shielding gas. This gas nozzle was directed opposite to the direction of travel at an angle of 30° with the work piece. During welding the work piece was placed horizontally on stainless steel backplate. There was a 5.0 mm $\times$ 5.0 mm square groove between the work piece and back plate under the weld region. Both the work piece and the backplates were clamped on a working table. The welding was carried out by moving the laser beam. Helium was used as the shielding gas with a flow rate of 94 l/min.

Weld samples were produced using a Nd:YAG laser unit with a maximum output power of 3 kW. The welding speeds were in the range of 48–121 mm/s. Three sets of weld samples were prepared using nominal laser powers of 1.0, 1.5, and 3.0 kW. The actual output powers, measured using a LM500 Coherent Labmaster device, were 0.9, 1.55, and 2.52 kW for nominal powers of 1.0, 1.5, and 3.0 kW, respectively. The focal point position of the Nd:YAG laser, determined with the help of a He–Ne red diode focusing laser, was kept at the surface of the plate during welding. The focal length of the He–Ne laser was 0.104 in. (2.64 mm) shorter than that of the Nd:YAG laser. In order to position the focal point of the Nd:YAG laser on the top surface of the specimen, a plate of 0.104 in. thickness was placed on the specimen table and the elevation of the laser head was adjusted to focus the He–Ne laser on the stainless steel plate surface. Then the original specimen table surface without the stainless steel plate was taken as the focal point for the Nd:YAG laser.

An additional set of experiments was conducted to test the influence of defocusing on the geometry of the weld and pore formation, using nominal laser power of 1.5 kW and welding speed of 105.8 mm/s. During this set of experiments the focus of the laser beam was positioned at defocus values in the range of -3.5 to $+3.0$ mm below (negative defocusing) and above (positive defocusing) the surface of the plates so that the laser power density varied in the range of approximately $9.6\times10^4-5.3\times10^5$ W/cm^2 as shown in Table II.

Metallographic samples were prepared using cold resin mounting and consequently polished with SiC paper and alumina powders down to 0.05 μm in size. Computer image analysis of the cross sections of the welds was performed using Image Pro® software to determine weld pool geometry and area percent and number density of pores in the weld pool. Some of the macrographs showing the weld pool geometry and macro pores were electronically enhanced to improve contrast. The microstructures in the weld metal were observed using optical microscopy and Vickers microhardness testing was conducted across the welds.

III. RESULTS AND DISCUSSION

A. Porosity

1. Influence of the welding speed and laser power

Figures 2(a), 2(b), and 2(c) shows the cross sections of laser welds produced on 2-mm-thick plates with welding speeds in the range of 53 to 121 mm/s at nominal powers of 3, 1.5, and 1.0 kW, respectively. The data show that randomly distributed macroporosity was always present in the weld pool and the base metal. The area percent porosity in the weld metal of both 2- and 6 mm thick plates for various welding conditions is shown quantitatively in Fig. 3. The average amounts of initial porosity in the base metals are also shown in this figure. It is observed that the amount of porosity decreased with the increase in welding speed. At low welding speeds, up to 40 area-percent porosity was present in the weld pool while at high welding speeds, the levels of porosity in the weld pools were comparable with those observed in the base metal. It is also observed in the figure that the decrease in laser power resulted in lower porosity in the weld pool. It will become apparent later in the article that the use of high welding speed and low laser

TABLE II. Power density at different beam defocusing for a laser power of 1.5 kW.

Beam defocusing (mm)	0	0.5	1.0	1.5	2.0	2.5	3.0	3.5
Power density (W/cm^2)	5.3×10^5	4.9×10^5	3.9×10^5	2.9×10^5	2.1×10^5	1.6×10^5	1.2×10^5	9.6×10^4

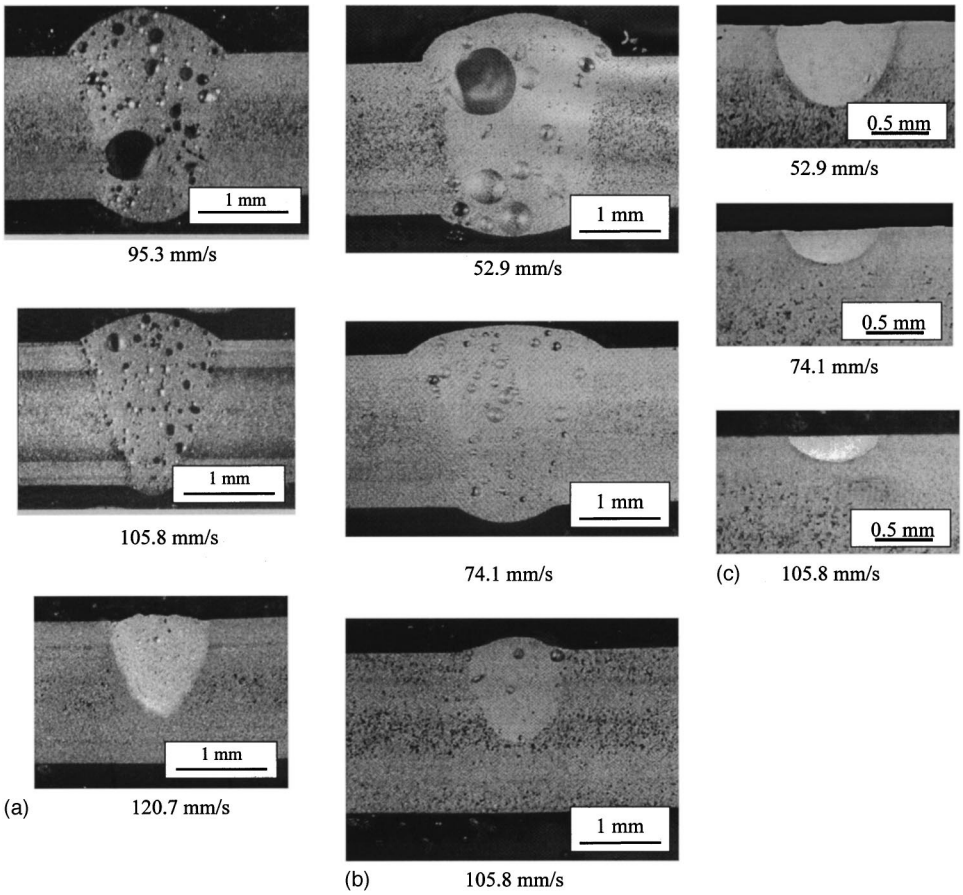

FIG. 2. Cross section of laser welds in 2 mm-thick plates of AM60B alloy at different welding speeds and laser powers.

power limited the time for pore growth and resulted in low level of porosity in the weld pool because of the high cooling rate during welding. However, the decrease in porosity at high welding speeds and low laser powers is accompanied by a concomitant reduction in the depth of penetration.

2. Influence of the beam defocusing

Figures 4(a) and 4(b) show the cross sections of welds produced at several defocus values in AM60B alloy of 2- and 6-mm-thick plates, respectively. The cross sections of the welds show that porosity was produced for all the defocusing conditions. The amount of porosity in the weld pool as a function of beam defocusing is shown in Figs. 5(a) and 5(b) for the 2- and 6-mm-thick plates, respectively. The initial porosity in the base metals is also shown in these two figures. It is observed that the amount of porosity in the weld pool does not change consistently with the change of beam defocusing. Therefore, porosity formation is less dependent on beam defocusing than on welding speed and laser power, i.e., the heat input which controls the cooling rate. It is also observed, comparing Figs. 5(a) and 5(b), that the porosity in the 2-mm-thick plates was less than that in the 6-mm-thick plates. This observation is consistent with the higher initial porosity in the 6 mm-thick plates than in the 2-mm-thick plates.

3. Mechanisms of porosity formation

The instability of the keyhole has been identified as one of the main causes of macroporosity during laser welding of

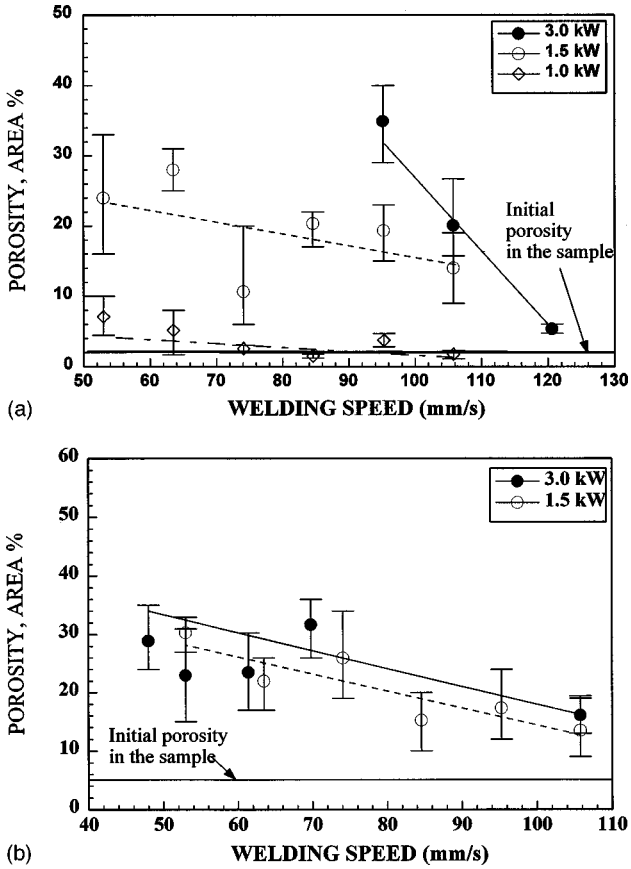

FIG. 3. Area-percent porosity produced in laser welds of AM60B alloy at several welding speeds and laser powers.

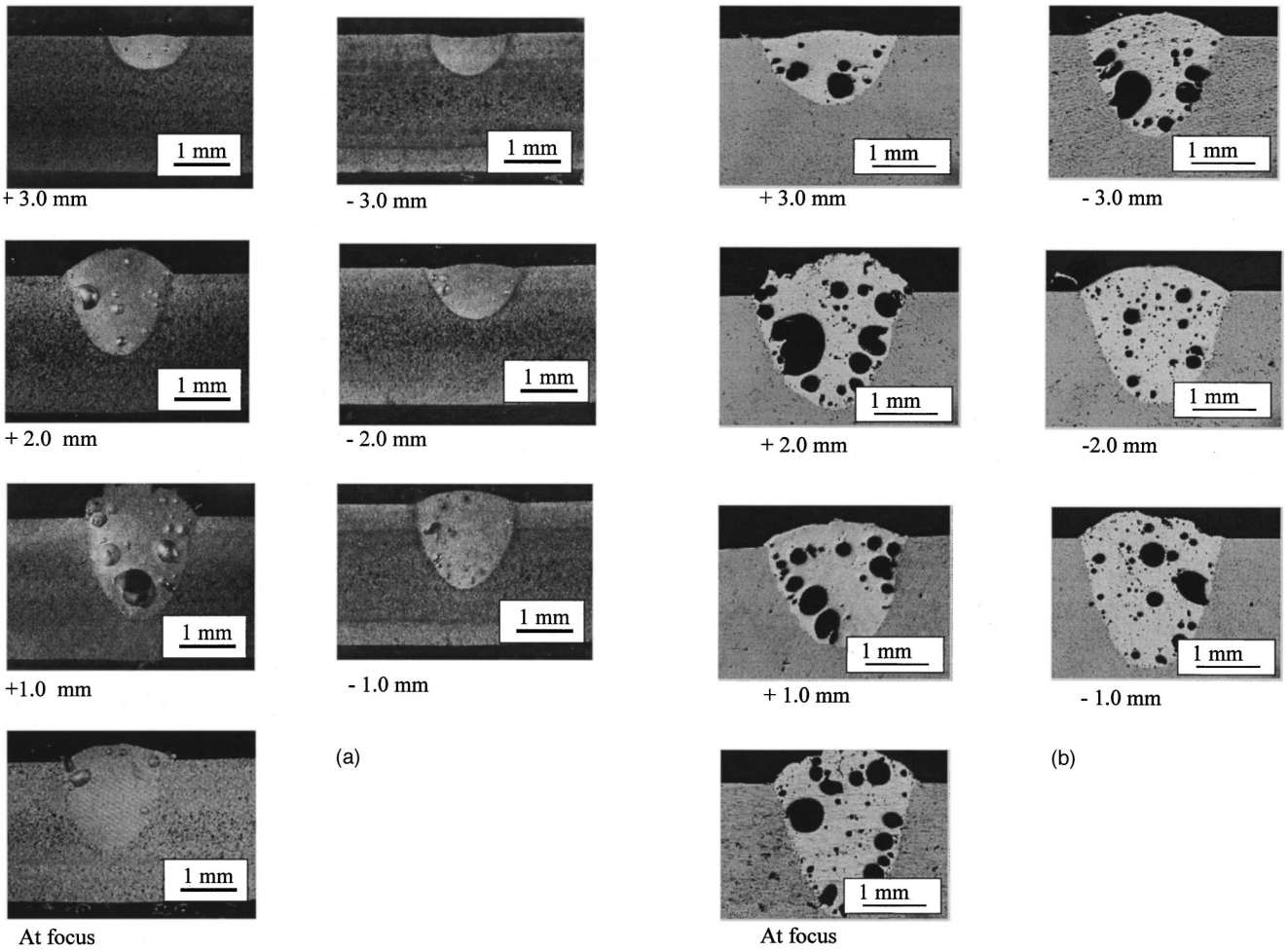

FIG. 4. Cross sections of laser welds produced at several beam defocus values.

many alloys.[11–16] Matsunawa *et al.*[13] studied the behavior of the keyhole during laser welding of aluminum and steel. A high-speed x-ray photographic method was used to observe the keyhole. They found that the depth and shape of the keyhole fluctuated violently during welding. These fluctuations caused large bubbles to be intermittently formed at the bottom of the keyhole. From their experimental observations they concluded that the non-uniform vaporization at the keyhole wall caused the instability of the keyhole and consequently, the formation of macropores in the weld metal.

Pastor *et al.*[15] showed the effect of keyhole stability on macropore formation during laser welding of automotive aluminum alloys with different extent of beam defocusing. A comparison of the area percent porosity versus the extent of defocusing for laser welding of AM60B alloy with 5754 aluminum alloy[15] shows that the welding mode, i.e., keyhole or conduction mode, for AM60B is not well defined and the amount of macroporosity cannot be related to the mode of welding. In contrast, during laser welding of 5754 alloy, the macroporosity is low in both stable keyhole mode and conduction mode welding as shown in Fig. 6.[15] In the range of welding variables for transition from conduction mode to keyhole mode, pronounced porosity is observed due to imperfect collapse of the keyhole. Therefore, in aluminum alloy 5754, macroporosity can be largely avoided by welding either in keyhole or in conduction mode of welding. However, macropores were constantly observed during laser welding of AM60B alloy, even when the penetration of the weld pool was very low characteristic of conduction mode welding. This indicates that the instability of the keyhole was not the main cause of porosity during laser welding of AM60B alloy.

Another possible cause of porosity in the weld metal is the preexisting porosity in the base metal.[1] The base metal used in this study is a die cast alloy that contains significant amount of macropores as shown in Fig. 7. The average amounts of porosity were 3.5 and 6.0 area percent in 2- and 6-mm-thick plates, respectively. Figure 8 shows geometry of several pores in the fusion zone near the fusion line. Some of the pores in this figure are not fully developed and the figure shows the process of pore formation. It is observed that near the fusion boundary, channels connect the large pores in the weld metal with the small preexisting pores in the solid base metal. During heating the gas from these small pores can expand into the large pores. This phenomenon is observed Fig. 8(a) which shows that an expanding pore near the center of the picture grows from an infusion of gas from small initial pores in the base metal. Figure 8(b) shows that a large pore was formed from the coalescence of several initial pores. The large pore located near the top of Fig. 8(c) indi-

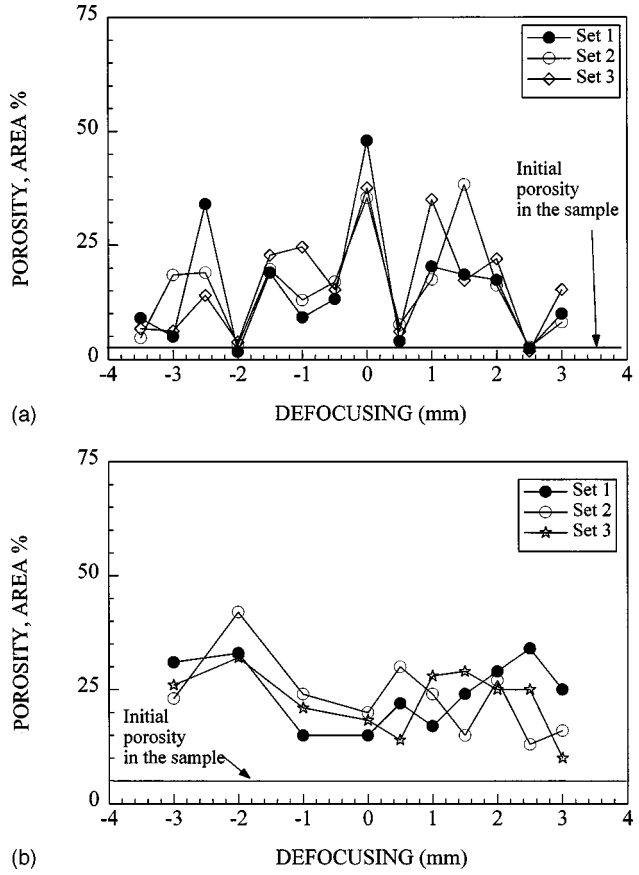

FIG. 5. Area-percent porosity produced in laser welds of AM60B alloy at several beam defocus values.

cates that it was growing from the expansion and coalescence of small pores. The elongated shape of this pore also indicates that the growth direction was from the fusion plane into the fusion zone. Figure 8(d) shows that the large spherical pore of about 0.6 mm diameter was formed at the center of the picture from the expansion of initial pores in the base metal. Therefore, the expansion and coalescence of the pre-existing pores were responsible for the formation of large pores in the weld metal.

The reason for the presence of porosity in the specimen can be traced back to the manufacturing of the die cast base metal. It is known that the solubility of hydrogen in liquid magnesium is much higher than in solid magnesium.[5] Upon

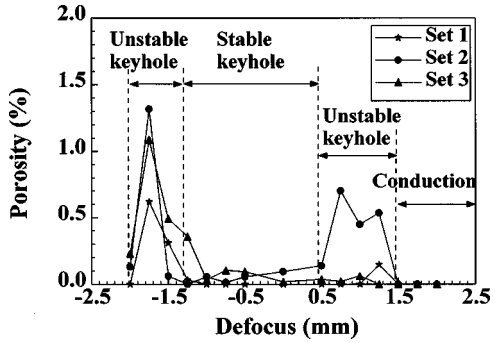

FIG. 6. Porosity produced in laser welds of 5754 aluminum alloy at several defocus values (see Ref. 15).

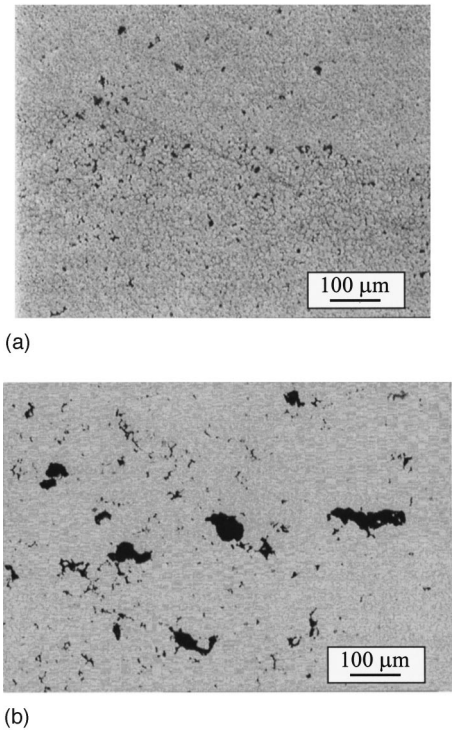

FIG. 7. Micrographs showing porosity in the AM60B base metal.

solidification, the solubility of hydrogen in the metal reduces drastically and the extra hydrogen is rejected from the metal, resulting in the formation of hydrogen gas bubbles. During die casting, the liquid metal is rapidly squeezed into the mold by a high pressure of up to 140 MPa.[18] The surface of the die cast metal solidifies very quickly and most of the gas bubbles are entrapped inside the metal, resulting in the formation of initial pores. Due to the application of high pressure during die casting, the gas pressures in the initial pores can be higher than one atmosphere. When the metal is re-melted during welding, the gas in the pores expands to release the pressure and contributes to the formation of large pores in

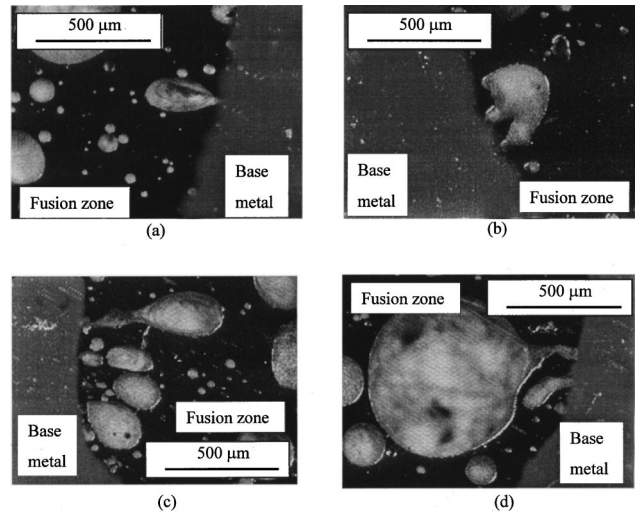

FIG. 8. Cross sections of welds depicting the mechanisms of pore formation near the fusion line of the weld pool.

TABLE III. Number density of pores in the weld pool and the base metal.

	Laser power	
Welding speed	1.5 kW	3.0 kW
52.9 mm/s	19 mm^{-2}	
63.5 mm/s	17 mm^{-2}	
74.1 mm/s	33 mm^{-2}	
85.6 mm/s	30 mm^{-2}	
95.3 mm/s	36 mm^{-2}	22 mm^{-2}
105.8 mm/s	39 mm^{-2}	33 mm^{-2}
120.7 mm/s		33 mm^{-2}
Base metal (2 mm thick)	224 mm^{-2}	

the weld pool. The expansion of initial pores results in higher total pore volume in the weld metal than that in the base metal as shown in Fig. 3.

The time for heating and coalescence decreases with increasing cooling rate in the weld pool. Therefore, the extent of initial pore expansion and consequently, the net increase in pore volume in the weld pool decrease with increasing welding speed and decreasing laser power. This trend can be observed in Fig. 3. Therefore, the use of high welding speed, low laser power, or any other measure to increase the cooling rate of the weld pool can control the expansion of the initial pores and minimize porosity formation in the weld pool.

The coalescence of the initial pores contributed to the increase in the average pore size but not to the net increase in the amount porosity in the weld pool. The coalescence process is expected to result in smaller number density of pores in the weld pool than in the base metal. As shown in Table III, the number density of pores decreased from 224 mm^{-2} in the 2-mm-thick base metal to values in the range of 17–39 mm^{-2} in the weld pools. It is also observed in Table III that the number density of pores in the weld pool increases with increasing welding speed and decreasing laser power. Both increase in welding speed and decrease in laser power increase the cooling rate and reduce the time for pore to coalesce, resulting in high number density of pores in the weld metal. Thus, the expansion and coalescence of the initial pores in the base metal were the main causes of macropore formation in the weld pool during laser welding of AM60B alloy. Elimination of the initial pores in the base metal is vital to obtain porosity free weldments.

B. Weld geometry

Overfill is the region of the weld metal located above the original surface of the base metal as shown in Fig. 9. Figure 10 shows the area-percent of both overfill and porosity in the fusion zone produced at several welding speeds. It is observed that both area-percent overfill and area-percent porosity decrease with increasing welding speed. It is also found that the area-percent porosity is roughly equal to the area-percent overfill. On the other hand, when a weld does not contain a large amount of porosity, the upper surface of the weld has a smooth profile and no overfill is formed. This evidence indicates that overfill was caused by the displacement of liquid metal by the pores. Therefore, any measure that decreases porosity in the weld pool will reduce the overfill.

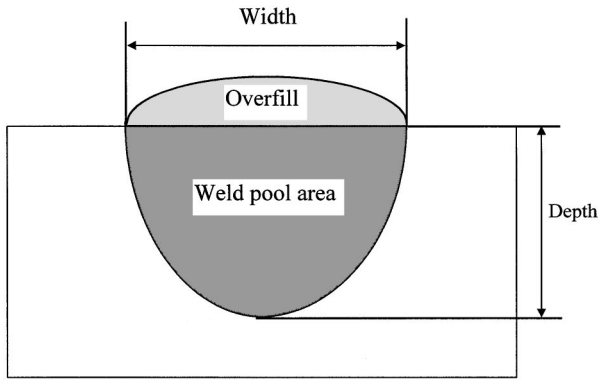

FIG. 9. Measurement of weld pool width, depth, and cross-section area.

As shown in Fig. 9, the weld pool depth and cross section area were measured without considering the overfill. The influences of welding speed and defocusing on the width, depth and cross-sectional area of the weld pool are shown in Figs. 11, 12, and 13, respectively. Each data point represents the average value of five measurements. As expected, the width, depth, and cross-sectional area of the weld pool decrease with increasing welding speed. It is observed that the weld pool geometry does not change significantly when the beam defocusing is in the range of −3 mm to +3

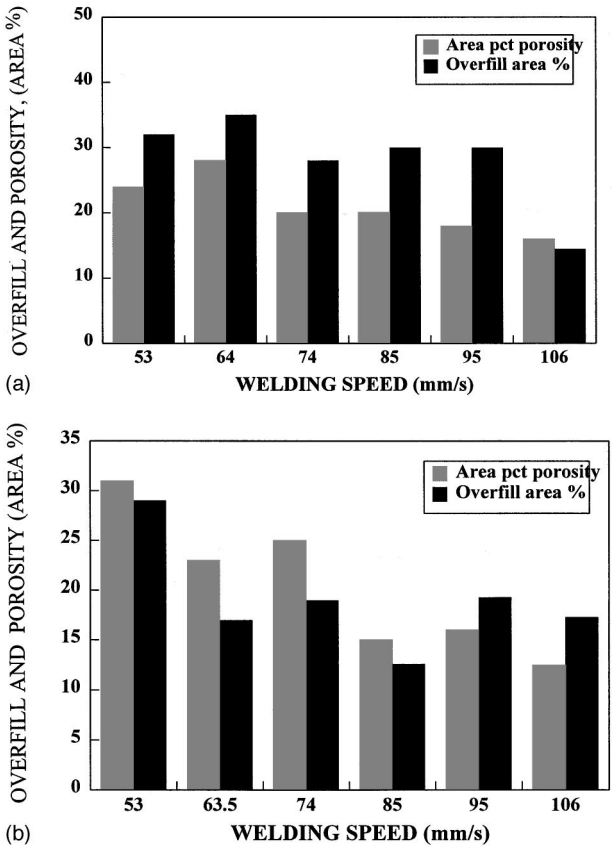

FIG. 10. Area-percent porosity and area-percent overfill in laser welds of AM60B alloy at several welding speeds.

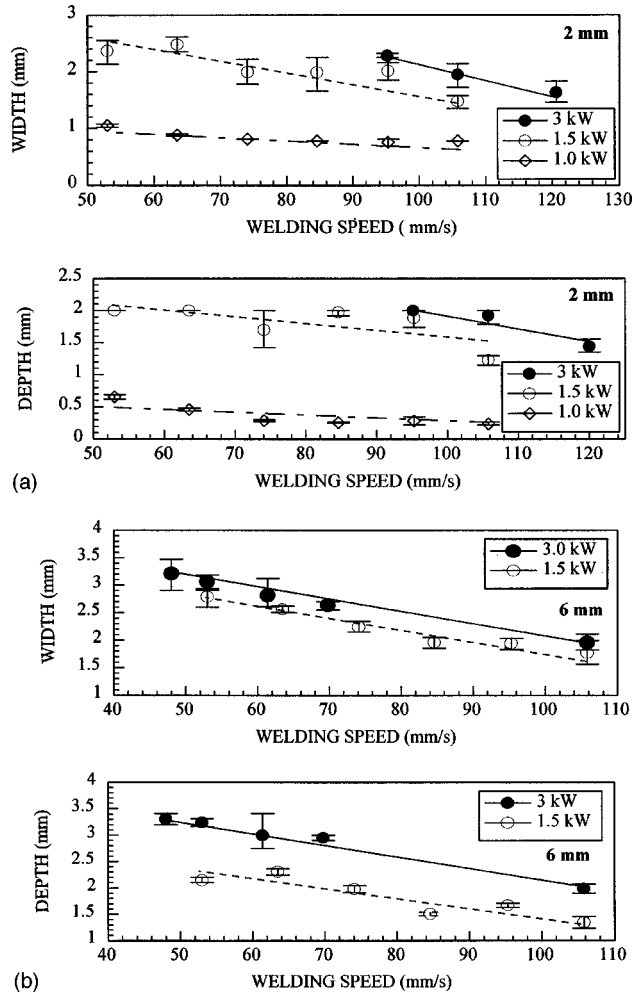

FIG. 11. Width and depth of the weld pools produced at several welding speeds and laser powers in AM60B alloy.

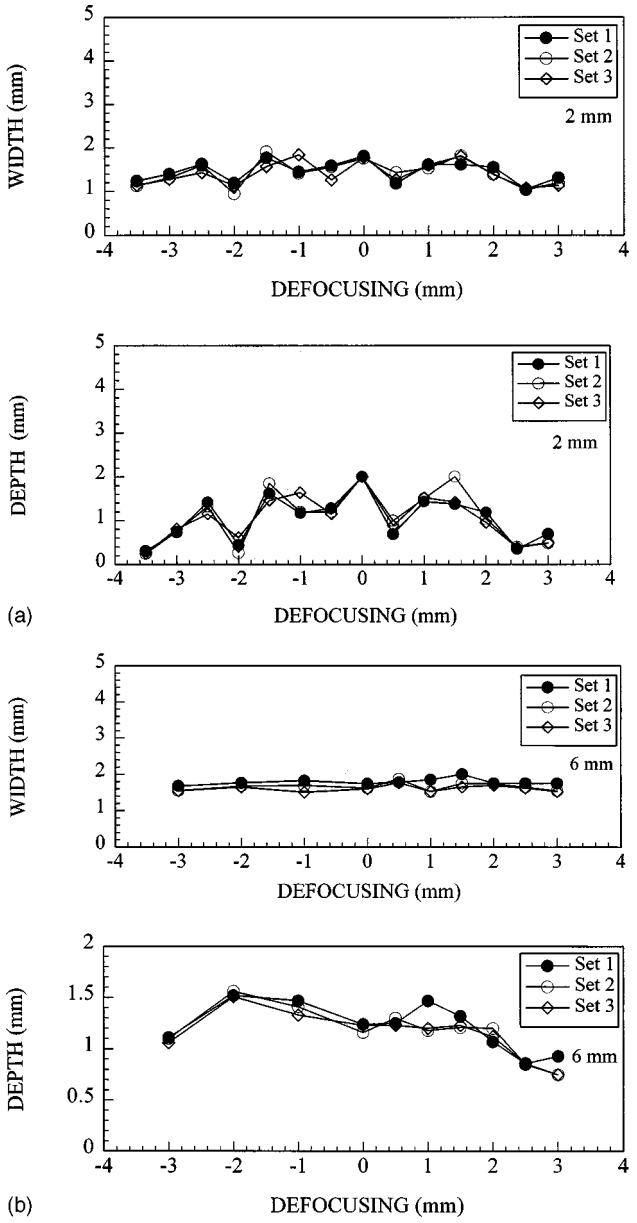

FIG. 12. Width and depth of the weld pools produced at several beam defocus values.

mm, which corresponds to an average laser power density in the range of $1.2\times10^5-5.3\times10^5$ W/cm^2. The deep penetration of these weld pool indicates that a keyhole was formed during the welding. When the beam defocus values are higher than $+3$ mm or less than -3 mm, i.e., the laser power density is smaller than 1.2×10^5 W/cm^2, the weld pool depth reduces more significantly than the weld pool width, resulting in shallow weld pool shape that is characteristic of conduction mode of welding. Therefore, the threshold laser power density for keyhole formation for this alloy is about 1.2×10^5 W/cm^2. This is much smaller than that for laser welding of 5000 series automotive aluminum alloys where the threshold values were in the range of $3.7\times10^5-8.4\times10^5$ W/cm^2.[15] This difference can be attributed to the much higher equilibrium vapor pressure of magnesium than that of aluminum.

C. Microstructure and hardness

Figure 14 shows the typical microstructures of the fusion zone and the base metal near the fusion plane. Heat affected zone is very small in the welds, which is characteristic of high power density laser welding. It is observed that the microstructures in both fusion zone and base metal consist of cored grains of magnesium-rich solid solution (gray) surrounded by $Mg_{17}Al_{12}$ (unetched) intermetallic compound at the grain boundaries. The volume fraction of $Mg_{17}Al_{12}$ intermetallic phase in the fusion zone is somewhat higher than that in the base metal, caused by the nonequilibrium solidification during the welding. Porosity (black) is present in both the fusion zone and the base metal. More porosity is observed near the fusion plane than in the interior, indicating pronounced rejection of hydrogen along the solid–liquid interface.

The solid solution phase has equiaxed morphology in the base metal and the fusion zone of low-speed welds as shown in Figs. 15(a) and 15(b), respectively. However, the morphology became dendritic in the fusion zone of 6-mm-thick plates at welding speeds higher than 74 mm/s as shown in Fig. 15(c). The grain size in the base metal is much larger than that in the fusion zone. The average grain size in the

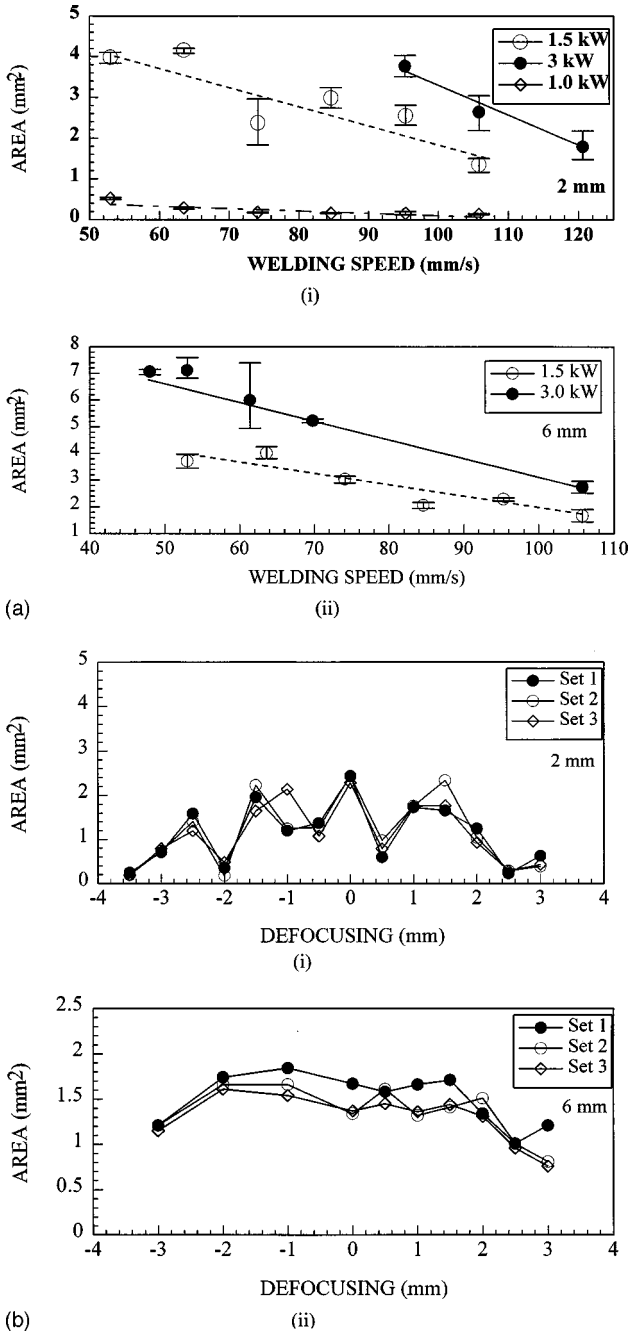

FIG. 13. Weld pool area produced at several welding speeds, laser powers, and beam defocus values.

base metal was about 30 μm while the average grain size in the fusion zone as a function of the welding speed is shown in Fig. 16. It is observed that for the 2-mm-thick plates, the average grain size in the fusion zone decreases as the welding speed increases as expected. For the 6-mm-thick plates, the grain size in the fusion zone also decreases with increasing welding speed of up to 74 mm/s. However, when the welding speed is higher than 74 mm/s, the morphology changes from equiaxed to dendritic and therefore, the grain size cannot be measured in terms of grain diameter. It is also observed that the grain size in the fusion zone of the 6-mm-thick plates is much smaller than that in the 2-mm-thick plates. The difference in grain size and grain morphology

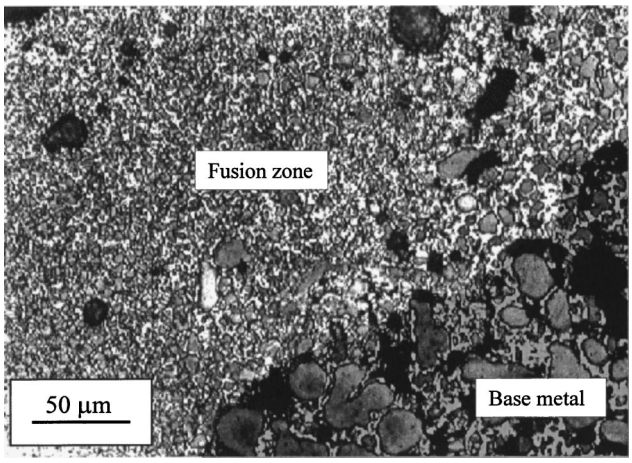

FIG. 14. Microstructures in fusion zone and base metal of laser welded AM60B alloy.

between these plates indicates that the cooling rate in the weld pool of 2-mm-thick plates was smaller than that of 6-mm-thick plates.

Vickers microhardness profile across the weld is shown in Fig. 17. This figure depicts an average hardness of about 53 H V in the base metal and 63 H V in the fusion zone. The

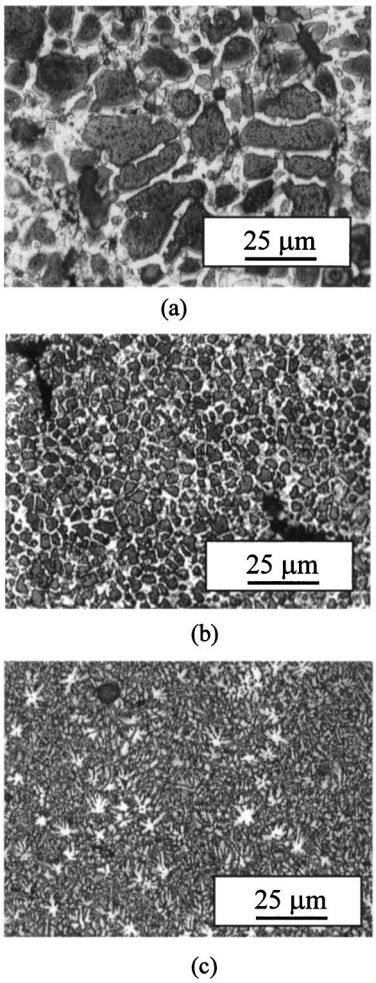

FIG. 15. Grain morphologies in the base metal and fusion zone of laser welded AM60B alloy.

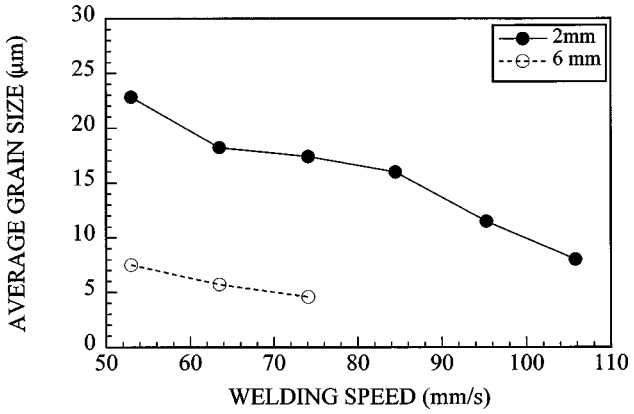

FIG. 16. Variation of grain size in the fusion zone as a function of the welding speed for laser welds of AM60B alloy.

small grain size and high volume fraction of $Mg_{17}Al_{12}$ intermetallic phase in the fusion zone are considered to be the main causes of hardening in the fusion zone. There is a narrow region in the base metal adjacent to the fusion line where the average hardness is lower than both the base metal and the fusion zone. The average hardness obtained from ten indentations in a region within 100 μm from the fusion plane was about 47 HV. The low hardness is considered to be caused by the accumulation of pores in this region. As shown in Fig. 18, low hardness values were obtained in regions of high porosity. Thus, the formation of porosity remains a major concern for the laser welding of AM60B alloy.

IV. CONCLUSIONS

This study shows a limited weldability of AM60B magnesium alloy due to the presence of initial pores in the base metal during laser welding. The major conclusions of this research are as follows:

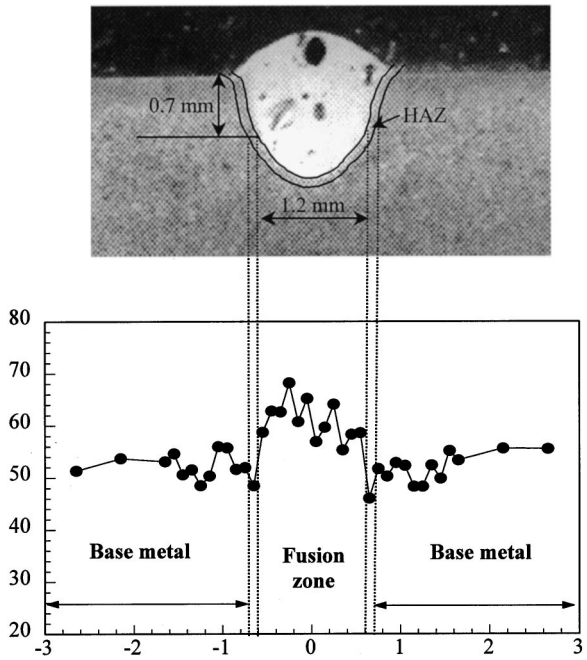

FIG. 17. Microhardness profile across the fusion zone of laser welded AM60B alloy.

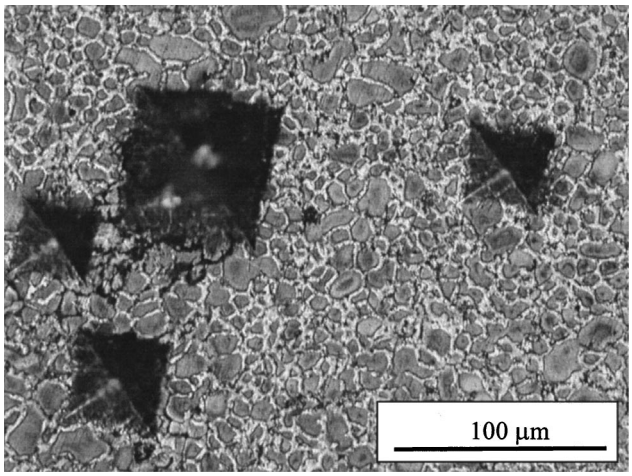

FIG. 18. Dents of microhardness testing showing the influence of porosity on hardness.

(1) Pronounced porosity in the fusion zone was observed under all the experimental conditions. The most dominant mechanism of porosity formation was expansion and coalescence of the initial pores in the base metal.

(2) Extent of porosity in the weld pool could be lowered to approximately that of the base metal by decreasing heat input, i.e., by either increasing welding speed at constant power or reducing power level at constant welding speed. However, the depth of penetration was reduced at low heat input.

(3) Initial pores in the base metal played a major role in the formation of macropores in the weld pool. It is essential to eliminate initial pores in order to obtain porosity free welds.

(4) Significant overfill was caused by the formation macroporosity in autogenous deep penetration welds. The extent of overfill could be lowered by reducing heat input.

(5)The power density needed for the formation of keyhole in AM60B was significantly lower than that necessary for the welding of 5000 series automotive aluminum alloys. The reduction in the threshold power density resulted from relatively higher equilibrium vapor pressure of the magnesium alloy.

(6) The microstructures of both the fusion zone and the base metal in the fusion consisted of a magnesium-rich solid solution and $Mg_{17}Al_{12}$ intermetallic. The hardness in the fusion zone was somewhat higher than in the base metal. This is considered to be caused by the small grain size and high volume fraction of $Mg_{17}Al_{12}$ intermetallic in the fusion zone.

ACKNOWLEDGMENTS

The authors thank Dr. D. White of Ford Motor Company for the donation of the alloy used in this study. The research was funded by the US Department of Energy (Grant Nos. DE-FG02-96ER45602 and DE-FG02-84ER45158).

[1] H. Haferkamp, Fr.-W. Bach, I. Burmester, K. Kreutzburg, and N. Niemeyer, in *Nd:YAG Laser Beam Welding of Magnesium Constructions, Proceedings of the Third International Magnesium Conference*, edited by G.

W. Lorimer (The Institute of Materials, Cambridge, UK, 1997), pp. 89–98.
[2] A. Weisheit, R. Galun, and B. L. Mordike, ''CO_2 Laser Beam Welding of Magnesium-Based Alloys,'' Weld. J. (Miami) **77**, 149s–154s (1998).
[3] P. G. Sanders, J. S. Keske, K. H. Leong, and G. Kornecki, ''High Power Nd:YAG and CO_2 Laser Welding of Magnesium,'' J. Laser Appl. **11**, 96–103 (1999).
[4] W. A. Baeslack III, S. J. Savage, and F. H. Froes, ''Laser-weld Heat-affected Zone Liquation Cracking in a High-strength Mg-based Alloy,'' J. Mater. Sci. Lett. **5**, 935–939 (1986).
[5] M. Avedesian and Hugh Baker, *Magnesium and Magnesium Alloys* (ASM International, Materials Park, OH, 1999).
[6] J. D. Shearouse III and B. A. Mikucki, The Origin of Porosity in Magnesium Alloy AZ91, Attributes of Magnesium for Automotive Design, International Congress and Exposition, Detroit, MI, February 28–March 3, 1994, pp. 53–63.
[7] S. Katayama, J. Light Metal Welding and Construction, **34**, 199–209 (1996).
[8] I. Masumoto and M. Kutsuma, International Institute of Welding, IIW Doc. IV, pp. 566–591, 1991.
[9] M. Kutsuma, Welding in the World, IIW31, pp. 126–135, 1993.
[10] R. A. Woods, in *Hydrogen in Metals*, edited by I. M. Bernstein and A. W. Thompson (ASM International Materials Park, OH, 1974), pp. 713–725.
[11] D. A. Schauer and W. H. Giedt, Weld. J. (Miami) **57**, 189s–195s (1978).
[12] R. P. Martukanitz and D. J. Smith, Proceedings of the Sixth International Conference on Aluminum Weldments, AWS Conference, Cleveland, OH, 1995, p. 309–323.
[13] A. Matsunawa, J. D. Kim, N. Seto, M. Mizutani, and S. Katayama, J. Laser Appl. **10**, 247–254 (1998).
[14] A. Cybullski and Z. Mucha, Welding International **11**, 212–220 (1997).
[15] M. Pastor, H. Zhao, R. Martukanitz, and T. DebRoy, Weld. J. (Miami) **78**, 207s–216s (1999).
[16] T. Klein, M. Vicanek, J. Kross, I. Decker, and G. Simon, J. Phys. D: Appl. Phys. **27**, 2023–2030 (1994).
[17] J. S. Kim, T. Watanabe, and Y. Yoshida, J. Laser Appl. **7**, 38–46 (1995).
[18] W. G. Moffatt, *Handbook of Binary Phase Diagrams* (General Electric, Schenectady, NY, 1976).